Flow Turbulence Combust (2013) 90:621–644
DOI 10.1007/s10494-013-9445-0

Investigation of Mixing Models and Conditional Moment Closure Applied to Autoignition of Hydrogen Jets

A. J. M. Buckrell · C. B. Devaud

Received: 9 March 2012 / Accepted: 2 January 2013 / Published online: 20 February 2013

Abstract The present paper is focused on performing a thorough investigation of first order Conditional Moment Closure (CMC) including an inhomogeneous turbulent mixing model for the conditional scalar dissipation rate to predict autoignition. Autoignition of a hydrogen and nitrogen fuel mixture in a heated coflow of air is examined. A sensitivity analysis is proposed for the autoignition length with respect to the mixing field, as well as a comparison of the effects of the inhomogeneous turbulent and Amplitude Mapping Closure (AMC) mixing models. The choice of turbulence constants only change predicted ignition length by approximately 5 % when applied to the AMC mixing model. Predictions of ignition length performed by the inhomogeneous model are lower than that of the AMC model by up to 15 %. The current ignition predictions are in reasonable agreement with the experimental data and previous simulation results. Two of the four regimes observed experimentally are reproduced qualitatively. Further improvement may be gained by using large eddy simulation and a gradient model for the conditional velocity in the inhomogeneous turbulent mixing model.

Keywords Conditional moment closure · Autoignition · Scalar dissipation rate · Turbulence · Combustion · Modelling

1 Introduction

Autoignition and subsequent flame propagation are crucial phenomena for many engineering applications such as those related to compression-ignition engines or fire safety. Further, increasingly stringent regulations on airborne pollutant emissions for transportation and power generation have prompted the search for alternative

A. J. M. Buckrell · C. B. Devaud (✉)
Department of Mechanical and Mechatronics Engineering, University of Waterloo,
200 University Avenue West, Waterloo, ON, N2L3G1, Canada
e-mail: cdevaud@uwaterloo.ca

fuel-efficient and low-emission power generation systems. Fuel blends including hydrogen appear to have some potential towards emission reduction in engines. Thus, there is a need for the development of numerical tools capable of predicting autoignition and combustion in an unsteady and turbulent environment including detailed kinetics for various fuel blends. Complex interactions between the turbulent flow/mixing fields and chemistry take place and must be accurately reproduced in numerical simulations of autoignition. A detailed review on autoignition processes can be found in reference [1] including both experimental and numerical investigations. Within the framework of autoignition modelling, several approaches have been developed, for example, the flamelet model [2], Conditional Moment Closure (CMC) [3], Conditional Source term Estimation (CSE) [4], Presumed Conditional Moment (PCM) [5], One-dimensional turbulence (ODT) model [6] and Probability Density Function (PDF) methods [7], in Reynolds Averaged Navier-Stokes equation (RANS) or Large Eddy Simulations (LES). Direct Numerical Simulations (DNS) have been also used in the context of autoignition [8] and provides information that is not easily measurable through experimental methods, however still remain extremely computationally expensive for practical cases.

The present study examines the case of autoignition of a heated hydrogen (H_2) and nitrogen (N_2) fuel mixture in a heated coflow of air, following the experimental study of Markides and Mastorakos [9] using a CMC approach in RANS. Several experimental data sets exist for the same experimental set-up and fuel mixture, but differ depending on the values of the air and fuel exit velocities. Previous numerical work can be found using the experimental conditions and data with the fuel exit velocity much larger than that of air coflow. Among those, Michel et al. [5] implemented different versions of PCM in RANS for a constant air temperature and varying the fuel and air coflow exit velocities with reasonable agreement with the experiments. Sensitivity to the PCM formulation is observed for the ignition length prediction. LES-CMC is shown to give good agreement for autoignition with experimental results [10]. The no-ignition, random spot and flashback regimes noted in the experiments are well reproduced. The 2D DNS performed by Kerkemeier [11] investigates autoignition regimes using the same experimental set-up and all of the experimental regimes observed, no ignition, random spots, flashback and lifted flame, are produced by varying the coflow temperature. It is also found that the mixture fraction predictions are in good agreement with the distribution predicted by the β-PDF.

The current work considers the data set for air and fuel velocity equal to 26 m/s. A few numerical studies have also incorporated the same experimental conditions as those used in the current investigation, for example, using RANS-CMC [12], RANS-PDF [13] and LES-PDF [14, 15]. Patwardhan and Lakshmisha find that RANS-CMC do not yield realistic combustion temperatures, but with the modification of turbulence model constants, reasonable agreement with experimental results is achieved [12]. However, the modified turbulence constants are determined by comparing turbulent mixing flow predictions with inert flow data [16] leading to some possible uncertainties in the selected values of the constant in reacting flow conditions. Lee and Mastorakos apply a transported scalar PDF approach in RANS using a standard k-ϵ model for the turbulent flowfield [13]. They conclude that the ignition predictions are sensitive to the chemical mechanism used, however, much less to the mixing model used in the PDF transport equation. It is also found that

their predicted ignition lengths are overpredicted compared to the experimental values. The LES-PDF studies performed by Jones and co-workers [14, 15] and based on the Lagrangian PDF method successfully reproduce the random spots and flashback regimes and give good agreement between predicted ignition lengths and experimental values.

In CMC, additional transport equations for conditional species concentration and temperature (or enthalpy) are solved. In non-premixed turbulent combustion, mixture fraction is the conditioning variable. The advantage of the CMC method is that the fluctuations about the conditional averages are much smaller than fluctuations about unconditional averages. In many flows, these conditional fluctuations are sufficiently small that they can be neglected, leading to first order CMC [3]. The scalar dissipation rate, χ, represents the rate of mixing at the molecular level and is proportional to the mean square gradient of the scalar, Z, such as $\chi \equiv 2\ D\ \nabla Z \cdot \nabla Z$, where D is the molecular diffusivity of Z. Within the CMC framework, its conditional average at a particular value, η, of mixture fraction, ξ is of special interest with $\langle \chi | \eta \rangle = \langle D \nabla \xi \cdot \nabla \xi | \xi = \eta \rangle$. The angular brackets denote a conditional average over an ensemble of realizations of the flow, subject to the condition to the right of the vertical bar.

Accurate modelling of the Conditional Scalar Dissipation Rate (CSDR) is crucial, as it appears in both the conditional species transport and temperature equations. However, evaluation of $\langle \chi | \eta \rangle$ is not straightforward. Two of the most common models used for closure of $\langle \chi | \eta \rangle$ are Girimaji's model [17] and the Amplitude Mapping Closure (AMC) model [18], both of which are derived using the assumption of homogeneous turbulence. Most turbulent flows of interest are not homogeneous, in particular in developing transient turbulent flow conditions found in autoignition problems. This modelling discrepancy in CMC has prompted developments of several formulations relaxing the homogeneous turbulence assumption [19, 20]. Inhomogeneous turbulent mixing models have been implemented in RANS-CMC under steady conditions [21–24] and small differences could be noted in species predictions. Recently, two inhomogeneous mixing model formulations have been incorporated to CMC and applied to autoignition of high pressure methane jet. In contrast to steady-state CMC studies [21–24], it is found that inhomogeneous turbulent mixing model in CMC can have a significant impact on the ignition delay predictions [25].

In the present paper, the experimental autoigniting case of Markides and Mastorakos [9] is re-visited by carrying out a thorough investigation of first order CMC to predict autoignition and flame propagation for different regimes, i.e. by varying the air coflow temperature. In contrast to previous CMC work [12, 26], an inhomogeneous turbulent mixing model is included in a fully-coupled RANS-CMC code using the conservative form of the CMC equations discretized in finite volume. In particular, a sensitivity analysis is proposed for the autoignition length with respect to the turbulent mixing field, as well as a comparison of the effects of the inhomogeneous turbulent and AMC mixing models.

The objectives of the present study are (1) to quantify the effects of modifying the turbulent Schmidt number and the constant, $C_{\epsilon 1}$ in the k-ϵ turbulence model on mixing field and autoignition length predictions, (2) comparison of the use of homogeneous turbulence based mixing models and inhomogeneous turbulence based mixing models and (3) to examine the development of flame structure following

the autoignition event. First order closure is applied to the conditional source term. The vast majority of CMC studies consider first order closure only and have been successful in accurately predicting autoignition [16, 27–32]. One possible reason for this success is that first order closure is shown to be sufficient when there is a rapid decay of the CSDR below its critical value [33]. Implementation of higher order or doubly-conditioning methods are beyond the scope of this paper. These may still be needed but further investigation is also required to examine the benefits versus high demand of computational resources and closure of many new terms. Thus, currently, it is important to fully investigate the impact of the existing models in first order CMC before developing more complex CMC methods.

2 Conditional Moment Closure

2.1 Conditional Moment Closure equations

In this section, the CMC governing equations and assumptions are briefly summarized. For a given species α, the conditional average of the mass fraction Y_α is defined by

$$Q_\alpha(\eta, x_i, t) = \frac{\langle \rho Y_\alpha(x_i, t) | \xi(x_i, t) = \eta \rangle}{\rho_\eta}, \tag{1}$$

where Q_α is the conditional average mass fraction of species α, ξ is the mixture fraction, η is the sample space variable upon which the mixture fraction is conditioned, such that $0 \leq \eta \leq 1$, and $\rho_\eta = \langle \rho | \eta \rangle$ is the conditional density. The independent variables x_i and t, represent spatial location and time, respectively. The transport equation for Q_α is given by [3]:

$$\frac{\partial(Q_\alpha)}{\partial t} + \langle u_i | \eta \rangle \frac{\partial(Q_\alpha)}{\partial x_i} = \frac{1}{\langle \rho \rangle \widetilde{P}(\eta)} \frac{\partial}{\partial x_i} \left(\langle \rho \rangle \langle u_i'' y_\alpha'' | \eta \rangle \widetilde{P}(\eta) \right) + \frac{1}{2} \langle \chi | \eta \rangle \frac{\partial^2 Q_\alpha}{\partial \eta^2} + \frac{\langle \dot{\omega} | \eta \rangle}{\langle \rho | \eta \rangle}, \tag{2}$$

where a high Reynolds number and unity Lewis number are assumed. The conditional fluctuations of the diffusivity are also neglected. The first term on the Left Hand Side (LHS) of Eq. 2 represents the temporal rate of change of the conditional species mass fraction, while the second term represents the conditional transport by convection. The first term on the Right Hand Side (RHS) of Eq. 2 accounts for the transport due to turbulent flux, the second term represents the molecular mixing and the third term is the chemical source term. Several of the terms in Eq. 2 remain unclosed, including the conditional chemical source term, $\langle \dot{\omega}_\alpha | \eta \rangle$, the turbulent fluxes, $\langle u_i'' y_\alpha'' | \eta \rangle$, the conditional velocity, $\langle u_i | \eta \rangle$, and the PDF, $\widetilde{P}(\eta)$, which are all presented below. The final unclosed term is that of the CSDR, $\langle \chi | \eta \rangle$, and is presented in further detail in Section 2.2.

Closure of the conditional velocity, $\langle u_i | \eta \rangle$, is based on the linear model [3], such that there is a linear progression of the conditional velocity in the sample space. The linear model closure is supported by experimental data provided by Kuznetsov and Sabel'Nikov [34]. Mortensen [20] suggests that the gradient diffusion conditional velocity model of Pope [35] is a more appropriate model to use with the presumed

form β-PDF. However, the linear model is commonly used for simplicity [25]. The conditional chemical source term is modelled using a first order closure. The PDF, $\tilde{P}(\eta)$, is modelled using a clipped Gaussian formulation [36]. The turbulent fluxes are modelled with the gradient diffusion hypothesis [37], which, for a conserved scalar ϕ, is given by $\langle u_i'' \phi'' \rangle = -D_T \frac{\partial \phi}{\partial x_i}$. The turbulent diffusivity, D_T, is given by

$$D_T = \frac{C_\mu}{Sc_t} \frac{\tilde{k}^2}{\tilde{\epsilon}}, \tag{3}$$

where $\tilde{k}$ and $\tilde{\epsilon}$ represent the local mean turbulent kinetic energy and dissipation rate, respectively. The turbulent Schmidt number, Sc_t, is initially set to 0.7 [12], and C_μ is set to the commonly used value of 0.09.

2.2 Scalar dissipation rate modelling

The mean scalar dissipation rate, $\widetilde{\chi}$, is a measure of the level of mixing present in a turbulent flowfield. Closure of $\widetilde{\chi}$ developed by Peters is used [38]:

$$\tilde{\chi} = C_\chi \frac{\tilde{\epsilon}}{\tilde{k}} \widetilde{\xi''^2}. \tag{4}$$

The value of the constant of proportionality is entirely dependent on the flow. Janicka and Peters [39] found that a value of $C_\chi = 2.0$ provides good performance when considering an inert methane jet. Various other models have been suggested for closure of the mean scalar dissipation rate [37]; however, they are not used in the current implementation of the CMC equations and are beyond the scope of the present work.

The CSDR is a key term in CMC and two models are briefly reviewed, one based on homogeneous turbulence (AMC) and one derived from the PDF transport equation without assuming homogeneous turbulence.

2.2.1 Amplitude Mapping Closure (AMC)

AMC is a mixing model that was initially developed by O'Brien and Jiang [18]. This model has been used in many previous CMC autoignition studies [12, 16, 28, 29]. The AMC model is derived from the homogeneous PDF transport equation using the mapping closure solution for the scalar PDF in which the PDF initially has a double-delta distribution and relaxes to a Gaussian distribution. The CSDR takes the form

$$\langle \chi \,|\, \eta \rangle = \chi_0 G(\eta), \tag{5}$$

where $G(\eta)$ is determined by

$$G(\eta) = \exp\left\{-2\left[\mathrm{erf}^{-1}(2\eta - 1)\right]^2\right\}, \tag{6}$$

erf^{-1} being the inverse error function, and χ_0 is found by

$$\chi_0 = \frac{\tilde{\chi}}{\int_0^1 G(\eta)\tilde{P}(\eta)d\eta}. \tag{7}$$

The AMC produces symmetrical and bell-shaped profiles for the CSDR always centred on $\eta = 0.5$.

2.2.2 Mixing model based on inhomogeneous turbulence

Devaud et al. [19] developed a mixing model without assuming homogeneous turbulence. The newly developed expression is derived directly from the PDF transport equation of the conserved scalar mixture fraction, $\tilde{\xi}$. The first step in derivation of this model is the double integration of the PDF transport equation, shown in its original form as

$$\frac{\partial \langle\rho\rangle \tilde{P}(\eta)}{\partial t} + \frac{\partial}{\partial x_i}\left(\langle\rho\rangle\langle u_i|\eta\rangle \tilde{P}(\eta)\right) = \frac{\partial^2}{\partial \eta^2}\left(\frac{1}{2}\langle\rho\rangle \tilde{P}(\eta)\langle\chi|\eta\rangle\right). \tag{8}$$

For consistency with the CMC calculations, the linear conditional velocity model is also used in Eq. 8. Following the double integration of Eq. 8, the general form of the inhomogeneous model is obtained, yielding

$$\begin{aligned}\frac{1}{2}\tilde{P}(\eta)\langle\chi|\eta\rangle = &-\frac{1}{\langle\rho\rangle}\left(\frac{\partial\langle\rho\rangle\widetilde{I}_1(\eta)}{\partial t}\right) + \frac{-1}{\langle\rho\rangle}\frac{\partial}{\partial x_i}\left(\langle\rho\rangle\widetilde{u_i}\widetilde{I}_1(\eta)\right)\\ &+\frac{-1}{\langle\rho\rangle}\left(\langle\rho\rangle\frac{\widetilde{u_i''\xi''}}{\widetilde{\xi''^2}}\widetilde{I}_2(\eta)\right).\end{aligned} \tag{9}$$

In this equation, I_1 and I_2 are integral quantities defined as

$$\widetilde{I}_n(\eta) = \int_\eta^1 \left(\eta^0 - \eta\right)\left(\eta^0 - \tilde{\xi}\right)^{n-1}\tilde{P}(\eta^0)\mathrm{d}\eta^0, \tag{10}$$

where $n = 1$ or $n = 2$. The boundary conditions for these integrals in η-space are [19]

$$\begin{aligned}&\widetilde{I}_1(0) = \tilde{\xi}, \quad \widetilde{I}_1(1) = 0,\\ &\widetilde{I}_2(0) = \widetilde{\xi''^2}, \quad \widetilde{I}_2(1) = 0.\end{aligned} \tag{11}$$

In the range of $0 \le \eta \le 1$, these functions are monotonic with respect to η [19].

Further simplification of Eq. 8 is achieved through the use of the gradient diffusion hypothesis to replace $\widetilde{u_i''\xi''}$ with the substitution

$$\widetilde{u_i''\xi''} = -D_T\nabla\tilde{\xi}. \tag{12}$$

Following simplification, Eq. 9 becomes

$$\begin{aligned}\frac{1}{2}\tilde{P}(\eta)\langle\chi|\eta\rangle = &-\frac{1}{\langle\rho\rangle}\left(\frac{\partial\langle\rho\rangle\widetilde{I}_1(\eta)}{\partial t}\right)\\ &+\frac{-1}{\langle\rho\rangle}\frac{\partial}{\partial x_i}\left[-\langle\rho\rangle\widetilde{u}_i\widetilde{I}_1(\eta) + \frac{\langle\rho\rangle D_T\widetilde{I}_2(\eta)}{\widetilde{\xi''^2}}\frac{\partial\tilde{\xi}}{\partial x_i}\right].\end{aligned} \tag{13}$$

Rearranging Eq. 13 and applying the continuity and transport equations of $\tilde{\xi}$ yields

$$\frac{1}{2}\tilde{P}(\eta)\langle\chi|\eta\rangle = -\frac{\partial}{\partial t}\widetilde{I}_1(\eta) + \left[-\tilde{u}_i\frac{\partial \widetilde{I}_1(\eta)}{\partial x_i}\right] + \left[-D_t\frac{\partial\tilde{\xi}}{\partial x_i}\frac{\partial}{\partial x_i}\left(\frac{\tilde{I}_2(\eta)}{\widetilde{\xi''^2}}\right)\right] + \left(\frac{\tilde{I}_2(\eta)}{\widetilde{\xi''^2}}\right)\left[\frac{\partial\tilde{\xi}}{\partial t} + \tilde{u}_i\frac{\partial\tilde{\xi}}{\partial x_i}\right]' \tag{14}$$

Equation 14 is shown to be the most suitable form for finite volume discretisation [19].

3 Numerical Implementation

The computational code used in the present study is a RANS based CFD code with fully coupled CMC calculations. The differencing scheme used in the CFD calculations follows the hybrid method developed by Patankar [40]. Solution of the pressure-velocity equations is accomplished through the use of the SIMPLER algorithm [41]. Following the CFD calculations of the flowfield, the CMC calculations are performed.

Although previous studies have produced good agreement with experimental testing using uncoupled CFD/CMC calculations [16, 29, 42], the assumptions made in the formulation of the uncoupled calculations become invalid after the point of ignition. Simulation of a flame requires feedback to the CFD calculations. In the present code, this is done in the form of the mixture density, calculated from the enthalpy of the species present. The conditional temperature calculations occur at the end of each timestep. The calculated density is returned to the CFD portion of the code following the CMC calculations at the end of every timestep.

3.1 Turbulence modelling

The $k-\epsilon$ turbulence model is chosen for closure of the turbulence terms in the current study [43]. The implementation of this model is achieved by using the turbulent kinetic energy (k) transport equation, shown in Eq. 15 and its dissipation (ϵ) transport equation given in Eq. 16:

$$\overline{\rho}\frac{\partial\tilde{k}}{\partial t} + \overline{\rho}u_k\frac{\partial\tilde{k}}{\partial x_k} = \frac{\partial}{\partial x_k}\left[\left(\frac{\mu_t}{\sigma_k}+\mu\right)\frac{\partial\tilde{k}}{\partial x_k}\right] + \overline{\rho}P - \overline{\rho}\tilde{\epsilon}, \tag{15}$$

$$\overline{\rho}\frac{\partial\tilde{\epsilon}}{\partial t} + \overline{\rho}u_k\frac{\partial\tilde{\epsilon}}{\partial x_k} = \frac{\partial}{\partial x_k}\left[\left(\frac{\mu_T}{\sigma_\epsilon}+\mu\right)\frac{\partial\tilde{\epsilon}}{\partial x_k}\right] + C_{\epsilon1}\overline{\rho}P\frac{\partial\tilde{\epsilon}}{\partial\tilde{k}} - C_{\epsilon2}\overline{\rho}\frac{\tilde{\epsilon^2}}{\tilde{k}}, \tag{16}$$

with

$$\mu_T = C_\mu\overline{\rho}\frac{\tilde{k}^2}{\tilde{\epsilon}}. \tag{17}$$

The standard model constants, first proposed by Launder and Sharma [44], are given as

$$C_\mu = 0.09, \quad C_{\epsilon 2} = 1.44, \quad C_{\epsilon 2} = 1.92, \quad \sigma_k = 1.0, \text{ and } \sigma_\epsilon = 1.3. \tag{18}$$

The $k-\epsilon$ equation has many well known deficiencies [37]. For example, it tends to overpredict the spreading of round jets, which leads to a subsequent reduction in penetration length. Modification of the $C_{\epsilon 1}$ and $C_{\epsilon 2}$ constants is a common way of compensating for these deficiencies [29]. However, it has not been widely documented how the $k-\epsilon$ model performs under the present conditions, when both fuel and air coflow have the same velocity. Consequently, a thorough analysis is performed in this paper to evaluate the impact of Sc_t found in the turbulent diffusivity in Eq. 3 and $C_{\epsilon 1}$ included in Eq. 15 on the turbulent mixing field and subsequently on autoignition. It is also important to note that no experimental measurement for velocity or mixing field is available for the present experimental conditions.

3.2 CMC implementation

In many previous implementations of CMC, the conditional species transport equation, Eq. 2, is shown in non-conservative form using a Finite Difference discretisation [29, 33] . A potential improvement in continuity and conservativeness can be realized by the use of a Finite Volume (FV) discretisation [22]. The use of the FV discretisation allows spatial fluxes to be conserved through variations of grid spacing and this feature is important when large spatial gradients are present for the conditional averages. In the present work, a 2-D axisymmetric FV discretisation of Eq. 2 is used. Further details on the discretisation and implementation of the FV formulation of the CMC equation can be found in [22], including information on the use of the PDF ratio and the zero flux boundary condition.

CMC calculations can be very time consuming in comparison to the CFD calculations due increased number of equations to solve and numerical stiffness introduced by the species chemical source term. Due to the nature of the stiff ODE's involved in the chemical mechanism, the computational time required at this stage dominates the total calculation time. The stiff ODE's are solved using a numerical algorithm developed specifically for the problem of solving this type of chemical interaction. This solver, known as the Variable coefficient Ordinary Differential Equation (VODE) [45] solver is used exclusively for the CMC calculations. Any reduction in the effort required to solve these equations will therefore offer a noticeable improvement in the computational efficiency and usability of the code.

Additionally, the CMC calculation grid must be set up to completely encompass the desired physical location of reaction, which is not always known beforehand. In order to combat these drawbacks, a dynamic CMC grid is used to provide a significant increase in the efficiency of calculations.

The dynamic grid is formulated on the assumption that relevant chemical reaction will not occur outside a given range of $\tilde{\xi}$ values, such that

$$\eta_{\min} \leq \tilde{\xi} \leq \eta_{\max}. \tag{19}$$

In the present work, $\eta_{\min}$ and $\eta_{\max}$ are set to 0.0023 and 0.85, respectively. These two bounds are located very far from the value of most reactive mixture fraction

(between 0.04 and 0.09, see Fig. 5) and that of stoichiometric mixture fraction (0.184). The lower and upper bounds, $\eta_{\min}$ and $\eta_{\max}$, respectively, are chosen such that the range encompasses any potentially reactive mixture fractions. When the value of $\tilde{\xi}$ falls out of the range defined in Eq. 19, the CMC node is effectively turned off, and no calculations are performed at this location. The PDF ratio is set to zero, indicating that there is no flux across the CMC boundaries. This zero flux condition is set for all of the dynamic CMC grid boundaries to limit the region in which calculations are required. The active nodes are updated every timestep. The effects of the dynamic CMC grid are extremely noticeable at the early times of simulation and when there is very little fuel present in the domain. This is demonstrated in Fig. 1, which is taken from an autoignition simulation used in the present study. In Fig. 1a, the black area represents the active CMC nodes at an early timestep of $\tau = 0.5$ ms with approximately 10 % of the CMC nodes active, while Fig. 1b represents the active CMC nodes at a later timestep of $\tau = 2$ ms, with approximately 50 % of the CMC nodes active. As it can be quite clearly seen from Fig. 1, there is a significant difference in the number of cells included in the calculation. This allows specification of a large initial CMC domain without the associated increase in computational cost. Provided $\eta_{\min}$ and $\eta_{\max}$ are selected such that combustion does not occur at any of the CMC boundaries, there is no affect on the accuracy of the results. Although the exact computational time savings are highly dependent on the flow parameters and area of simulation, the additional flexibility and usability afforded by this feature make the model significantly more accessible to industry type usage as opposed to solely being used in research applications.

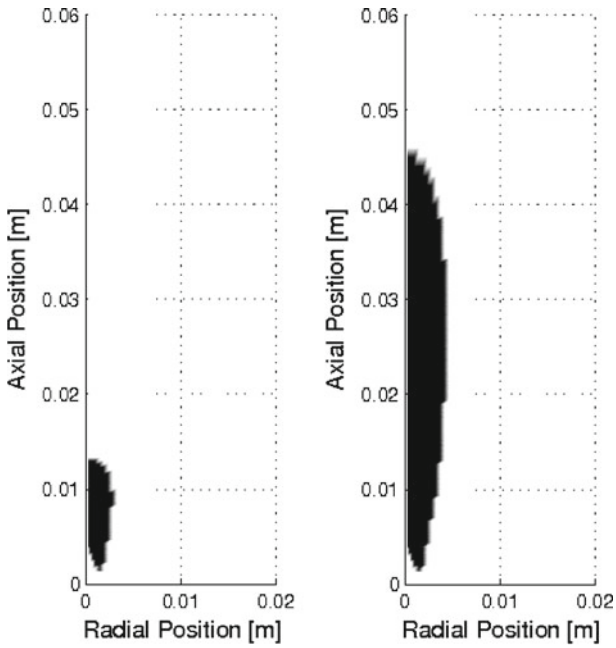

Fig. 1 Dynamic CMC grid, active CMC nodes are shown in *black*

The mixture fraction grid consists of 80 nodes, with 60 nodes placed between $\eta = 0$ and $\eta_{\text{stoich}} = 0.184$, and 20 nodes placed between $\eta_{\text{stoich}} = 0.184$ and $\eta = 1$. More nodes are clustered around the most reactive mixture fraction. The conditional averages are found to be grid independent with the present mesh.

3.3 Computational details

The computational domain closely follows the dimensions and geometric configuration of the experimental set-up [9]. The domain consists of a central jet of fuel and heated coflow of air in a quartz tube of 25 mm inner diameter. Therefore, the computational domain is composed of an axisymmetric slice representing the central burner, the coflow inlet, the wall of the quartz tube and the flow outlet. The simulation domain has a radius of 12.5 mm and a total length of 150 mm. The fuel and coflow inlets are placed along the base of the domain. The fuel inlet is located along the centreline, with the coflow inlet occupying the remaining area. In an effort to expand upon the available previous numerical studies, the same set of conditions used by Patwardhan and Lakshmisha [12], Jones and Navarro-Martinez [14] and Jones et al. [15] is applied to the simulations, allowing for the most direct comparison of results. The fuel inlet provides a fuel velocity of 26 m/s, and a fuel composition of $Y_{H_2} = 0.13$ and $Y_{N_2} = 0.87$. The fuel temperature is held constant at 750 K. The total width of the inlet matches the experimental diameter of 2.25 mm. It is separated from the coflow by an adiabatic wall representing the fuel tube. The coflow inlet boundary is modelled as an inlet of pure air, $Y_{O_2} = 0.232$ and $Y_{N_2} = 0.768$, extending from a radial coordinate of 1.445 mm (radius of fuel inlet outside diameter) to the domain radius of 12.5 mm. Depending on the scenario used for simulation, the coflow temperature is varied between 940 K and 1080 K, with the velocity held constant at 26 m/s. The conditions across both the fuel and coflow inlets provide a uniform distribution of flow parameters, such as velocity, temperature, density, etc. The turbulence intensity is set to 8 % for the simulations.

The outer boundary, representing the surface of the quartz tube containing the flow is modelled as an adiabatic, no-slip wall. This boundary condition most closely represents the flow, as during the experiments the apparatus is allowed to run until the temperature loss throughout the domain is minimal. The no-slip boundary condition is representative of the surface of the quartz tube, as there is no surface velocity.

The outlet is placed along the entire top boundary of the domain. The outlet boundary forces a zero gradient condition on any flow parameter, i.e. pressure, velocity, temperature, etc. Therefore, this boundary must be placed sufficiently far from the flow that this forced zero gradient does not impact the region of interest.

The final CFD/CMC computational grid consists of an axisymmetric, structured mesh with 195 cells in the axial direction and 29 cells in the radial direction. The area of finest mesh spacing yields cells of 0.3 mm $\times$ 0.3 mm. An aspect ratio of unity is targeted for areas near the inlet, and grid refinements are focused in areas with large gradients. In the present study, a fixed timestep of 1×10^{-6} s is selected. Flowfield and CMC values are output from the code every 5 timesteps (5×10^{-6} s). Iteration of the CFD flowfield continues until velocity and mass residuals of the flowfield converge below 1.0×10^{-4}.

Following previous investigations for the same flow conditions [12, 14, 15], the chemical mechanism used is that of Yetter et al. [46]. This mechanism consists of 19 steps with nine species. Testing performed by Stanković and Merci [47] and Lee and Mastorakos [13] indicates that although there is some sensitivity to the mechanism chosen, all mechanisms yield similar trends for ignition delay and most reactive mixture fraction, η_{mr}, defined as the mixture fraction where ignition first occurs in mixture fraction space.

The spatial grid, as well as simulation timestep are tested and the present results are determined to be grid and timestep independent.

Results shown in Section 4.1 are obtained from steady state calculations, whereas those in Sections 4.2, 4.3 and 4.4 (unless otherwise stated) are extracted from unsteady RANS where ignition is captured as a transient phenomenon occurring at a given time and spatial location.

4 Results

4.1 Sensitivity analysis related to the turbulent mixing field predictions

In the present simulations, several scenarios are tested in order to characterise the sensitivity of the turbulent mixing field to variation of the mixing (Sc_t) and turbulence model ($C_{\epsilon 1}$) constants. As the effects of the $k-\epsilon$ model have not been studied in the current flow to the same extent as with a standard jet flow [37, 43, 48, 49], it is not known what combination of turbulence constants will provide the most accurate flow simulation. No experimental data is available for comparison [9]. Thus, the current analysis is undertaken only to evaluate relative changes in the model, and not the absolute accuracy of the predictions. Three separate cases are undertaken in order to isolate the effects of mixing constants and to quantify how modifications of Sc_t and C_{ϵ_1} affect the mixing field. These cases are summarized in Table 1. Case 1 uses the standard turbulence and mixing constants. This is the baseline case for comparison purposes. Case 2 includes the modified value of $Sc_t = 0.5$ of Patwardhan and Lakshmisha [12]. Case 3 is undertaken to isolate the effect of C_{ϵ_1} modification on the mixing field: C_{ϵ_1} is equal to 0.4. Further increase in the value of C_{ϵ_1} from 1.44 is not included in the present study. It is shown that increasing C_{ϵ_1} from 1.44 to 1.6 could not improve the predicted spreading rate for a H_2-N_2 jet issuing into a vitiated coflow [50]. For each of the 3 cases given in Table 1, a steady state fully burning CMC simulation with $T_{\mathrm{coflow}} = 980$ K is run. The mixing field in each of the 3 cases is examined primarily to determine the $\tilde{\xi}$ and $\widetilde{\xi''^2}$ distribution within the flow. No analysis of the velocity field is provided, as the flow is largely absent of shear and velocity gradients.

As shown in Fig. 2, the centreline mean mixture fraction, $\tilde{\xi}$, values predicted by Case 1 are much larger than those given by Case 2 and 3, in particular in the region

Table 1 Sets of turbulence and mixing parameters used in autoignition simulations

Parameter case	C_{ϵ_1}	Sc_t
Case 1—Standard constants	1.44	0.7
Case 2—Modified C_{ϵ_1}	0.40	0.7
Case 3—Modified Sc_t	1.44	0.5

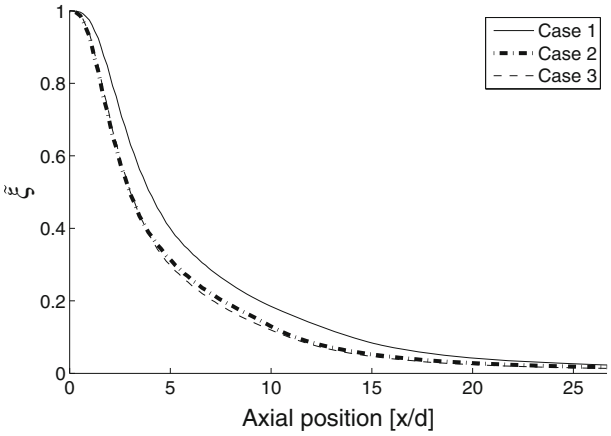

Fig. 2 Centreline $\tilde{\xi}$ profile

between x/d = 5 and x/d = 15. The difference in magnitude indicates that a higher level of mixing is seen along the centreline in Cases 2 and 3. Case 2 yields values 20–40 % lower than those in Case 1. Likewise, Case 3 predicts the centreline mean mixture fraction between 25 and 50 % smaller. Therefore, for a 72 % reduction of C_{ϵ_1} in Case 2, the difference in centreline $\tilde{\xi}$ ranges from approximately 20–40 % in the axial region investigated, while for a 29 % reduction in the value of Sc_t, a reduction of approximately 25–50 % is observed for this same region. This indicates that the predictions of $\tilde{\xi}$ are more sensitive to modification of Sc_t than modification of C_{ϵ_1}.

The centreline $\widetilde{\xi''^2}$ distribution presented in Fig. 3, shows much larger differences between cases than was seen with $\tilde{\xi}$ (Fig. 2). At the early stages of mixing, i.e. near the fuel inlet, between x/d = 0 and x/d = 3, Case 1 exhibits the lowest variance, with Case 2 and Case 3 predicting a larger variance value in this region. This large $\widetilde{\xi''^2}$ indicates that this is a very strong turbulent region of mixing, and this corresponds to the large gradient seen in mean mixture fraction near the inlet seen in Cases 2 and 3 (shown Fig. 2). Further downstream from the fuel inlet, between approximately x/d = 3 and x/d = 7, a significantly stronger peak in variance is seen for Case 2,

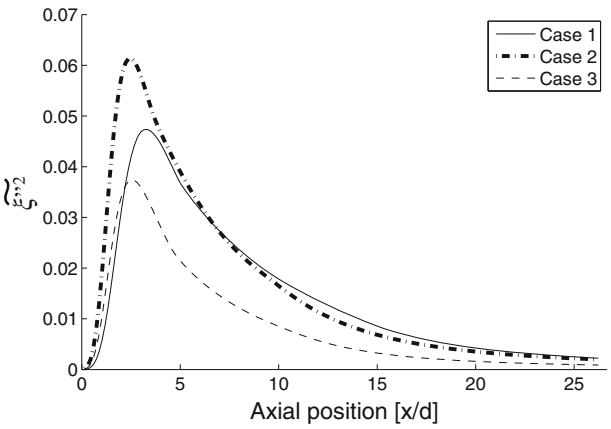

Fig. 3 Centreline $\widetilde{\xi''^2}$ profile

with an increase of approximately 30 % in comparison to the peak Case 1 baseline results. The variance predictions in Case 3, although larger than the values of Case 1 prior to x/d = 3, show an early peak and drop off, falling below the predictions of Case 1. The peak $\widetilde{\xi''^2}$ values seen in Case 3 are approximately 27 % lower than the peak predicted by Case 1. This pattern indicates that although both Cases 2 and 3 show strong initial mixing, the effects of the change in Sc_t with Case 3 are greatest near the inlet, and then decrease throughout the remainder of the domain, while modifications of C_{ϵ_1} have an effect throughout the majority of the domain. The current results are quantitatively and qualitatively similar to those seen using n-heptane as a fuel in a similar flow [16].

4.2 Sensitivity analysis related to the predictions of ignition length using AMC

The autoignition simulations conducted in the present study are divided into two major parts. The first part of the study provides a characterisation of the effects of temperature and turbulence constants on the autoignition conditions. The second part provides an investigation into the effects of mixing model for the CSDR in Eq. 2, and is presented in Section 4.3. This is conducted via the implementation of the inhomogeneous turbulent mixing model with the constants used in Case 1.

The autoignition length is a metric used in assessing the time it takes for a fuel in an unmixed state to mix with the oxidizer and reach the specified ignition criteria, which, in this study, is a 1 % increase in Favre-averaged temperature at a given instant. Other ignition criteria may be used but negligible differences are noted in the ignition predictions [26, 28]. In Fig. 4, results from the simulations undertaken in both the first and second parts of the study are summarized with the experimental measurements. At almost all temperatures, the largest L_{ign} is predicted by Case 2. Case 1, the baseline case, provides intermediate predictions, while Case 3 yields the shortest ignition lengths, correlating with the lowest $\widetilde{\xi''^2}$ predictions. At high temperatures, the difference between the cases is reduced, and all cases predict essentially the same value of L_{ign}. The reduction of L_{ign} with increasing T_{coflow}, and a corresponding reduction in the sensitivity to the selection of model constants indicates an increasing

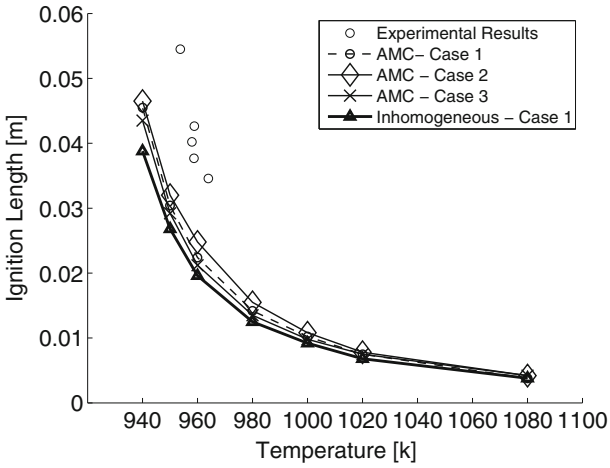

Fig. 4 Ignition length comparison for AMC and inhomogeneous mixing model with different mixing constants

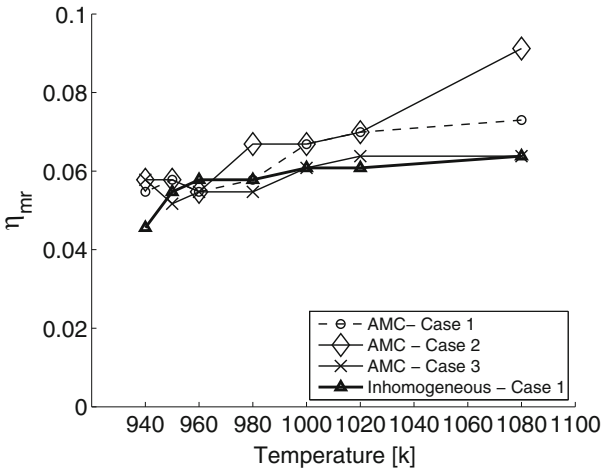

Fig. 5 η_{mr} comparison for AMC and inhomogeneous mixing model with different mixing constants

dominance of the chemical source term in the CMC equation. The effects of the mixing fields have less of an impact on ignition predictions in this high temperature region. For all cases the predicted values of L_{ign} stay within approximately 5 % using the AMC model.

Although the predicted values of L_{ign} stay within approximately 5 % for all simulations using the AMC model, the effects of turbulent constants is more clearly seen through analysis of η_{mr} in Fig. 5. In general, all of the cases tested show a tendency for η_{mr} to decrease with decreasing temperatures, especially as the "no ignition" experimental region is approached. This decrease at low temperatures, consistent with what is seen experimentally at the ignition limit, may be an indication of the chemical mechanism favouring lean mixture fractions for increased chemical activity. At higher temperatures, the value of η_{mr} becomes less sensitive to the coflow temperature. This is also in agreement with the findings of Stanković and Merci

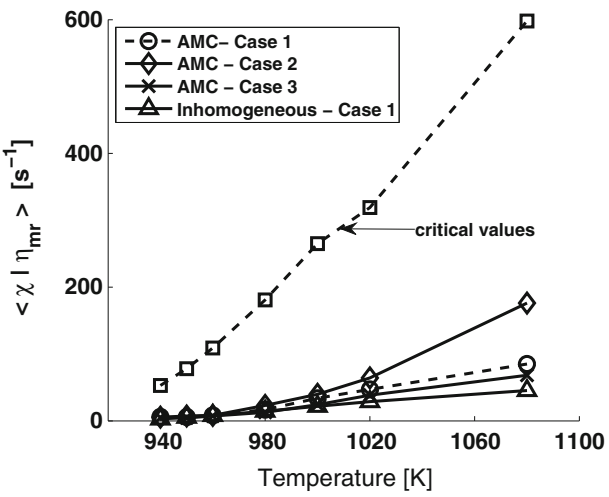

Fig. 6 $\langle \chi | \eta = \eta_{\mathrm{mr}} \rangle$ comparison for AMC and inhomogeneous mixing model with different mixing constants

[47], indicating that the region of peak chemical activity does not have a strong air coflow temperature dependence in the higher temperature region. Thus, this leads to the conclusion that autoignition is mostly chemistry controlled for high coflow temperatures.

As shown in Figs. 5 and 6, the highest values of η_{mr} and $\langle\chi|\eta=\eta_{\mathrm{mr}}\rangle$ are seen for Case 2 with the AMC mixing model for air coflow temperatures above 960 K. As this corresponds to the highest centreline $\widetilde{\xi''^2}$ seen in Fig. 3, it follows that an increase in $\widetilde{\xi''^2}$, and therefore $\tilde{\chi}$, favours a higher η_{mr} at the time of ignition. The Case 1 baseline provides the next highest predictions of η_{mr} and $\langle\chi|\eta=\eta_{\mathrm{mr}}\rangle$, with Case 3 providing the lowest predictions. This trend follows what is observed for centreline $\widetilde{\xi''^2}$, with the largest values for Case 2 and smaller values for Cases 2 and 3. As a general trend, it can be observed that as T_{coflow} decreases, the values of η_{mr} and $\langle\chi|\eta=\eta_{\mathrm{mr}}\rangle$ decrease sharply. Although there was no instance in the present study in which ignition was not observed to occur, the sharp downward trends with decreasing temperature indicate that the "no ignition" boundary is close to the minimum value of $T_{\mathrm{coflow}}=940$ K used in the simulations. These trends are explained by the dependence of the conditional chemical source term, $\langle\dot{\omega}_\alpha|\eta\rangle$ in Eq. 2, on T_{coflow}. At low temperatures, $\langle\dot{\omega}_\alpha|\eta\rangle$ is a smaller magnitude and still needs to balance the effects of mixing, convection and diffusion. Therefore the timescales associated with ignition are larger and of a similar order to the mixing timescales, meaning that the predictions of $\langle\chi|\eta\rangle$ have a larger influence on L_{ign}. At high temperatures, the magnitude of $\langle\dot{\omega}_\alpha|\eta\rangle$ is larger, and the associated timescales with the ignition process decrease. As a result, the ignition predictions become less dependent on the mixing field. This is demonstrated by the spread of L_{ign} predictions at low temperatures, which range approximately 3 mm from largest to smallest, while at higher temperatures, the difference in ignition length prediction between cases is reduced to approximately 0.5 mm.

4.3 Comparison between AMC and turbulent inhomogeneous model results

This section provides a detailed comparison between the results obtained with both the AMC and inhomogeneous mixing models. Predicted ignition lengths and conditional values are provided for both models at $T_{\mathrm{coflow}}=980$ K. Results were also processed at $T_{\mathrm{coflow}}=1080$ K and $T_{\mathrm{coflow}}=950$ K [51] but are not presented for brevity. Similar conclusions were found for coflow temperatures of 1080 and 950 K. In this section, the temporal evolution of the CSDR, the conditional species mass fractions and conditional temperature is examined.

4.3.1 Predictions of ignition length

As shown in Section 4.2, the choice of turbulence constants only leads to a difference of approximately 5 % in the predictions of ignition length when using the AMC mixing model. Upon simulation with the inhomogeneous mixing model, the ignition length is seen to decrease throughout the domain, especially at lower T_{coflow}, as shown in Fig. 4. The L_{ign} results from the inhomogeneous model stay within approximately 15 % of Case 1 predictions with the AMC model for the range of coflow temperatures tested. It is seen that the difference between mixing model predictions is largest for low T_{coflow}. This is consistent with higher sensitivity of autoignition to mixing for low air coflow temperatures, as observed in Section 4.2. The present results are in agreement with those of Milford and Devaud [25] where much larger

differences in predicted ignition delay between homogeneous and inhomogeneous models were noted if the gradient diffusion model was used for the conditional velocity.

The flow conditions at which ignition occurs are seen to be slightly different depending on the mixing model chosen. In Fig. 5, Case 1 results for the AMC model and the inhomogeneous model display similar trends, while the predicted values of η_{mr} for the inhomogeneous model remain slightly lower in magnitude. The temperature dependence at low T_{coflow} is again demonstrated, with an increase in the value of η_{mr} as temperature increases, while at higher temperatures this dependence is not seen. The same mechanism responsible for this trend with the AMC model is also responsible for the predictions of the inhomogeneous model: as the temperature increases, the rate of reaction increases, seen with a larger chemical source term in the CMC equation, and the ignition process is controlled less by mixing and more by time available for reaction to occur, resulting in similar values regardless of the model and constants chosen.

Critical values for the CSDR above which no ignition can occur, are also shown in Fig. 6. These values are obtained by performing some flamelet-type calculations, i.e. spatial transport is not included in Eq. 2. At a given air coflow temperature, the scalar dissipation is progressively increased until ignition becomes impossible. Following the same methodology as in previous work [28], the AMC model is used and only χ_0 in Eq. 5 is increased. From a critical value of χ_0 a critical value of CSDR can be determined. As can be seen in Fig. 6, it is clear than ignition always occurs at low CSDR values, much lower than the critical values, whatever model used. This is in agreement with previous studies on autoignition [16, 28]. This can also explain the limited impact on ignition of the inhomogeneous mixing model compared to AMC. The inhomogeneous model is expected to have a larger effect on ignition when the CSDR is close or above the critical value.

4.3.2 Conditional scalar dissipation rate temporal evolution

Since the values for mixture fraction, velocity and related variance of both the AMC model and inhomogeneous model are identical up to the point of ignition, any differences in the ignition predictions by the CMC equation, Eq. 2, are due to the evolution of $\langle \chi | \eta \rangle$. The AMC model provides bell-shaped distributions of $\langle \chi | \eta \rangle$, centred at $\eta = 0.5$. In the inhomogeneous model, the shape of $\langle \chi | \eta \rangle$ is not pre-defined, and may vary with time and location following the solution of Eq. 13.

In Fig. 7a, a temporal evolution of $\langle \chi | \eta = \eta_{\mathrm{mr}} \rangle$ is shown for the different mixing models. It is immediately apparent that the choice of model provides a large difference in the $\langle \chi | \eta = \eta_{\mathrm{mr}} \rangle$ evolution. At times leading up to ignition, the AMC model is seen to predict large initial values followed by a decrease, while the inhomogeneous model predicts a steady increase. At the time of ignition, both models predict similar values of $\langle \chi | \eta = \eta_{\mathrm{mr}} \rangle$.

In Fig. 7b and c, the respective curves for $\langle \chi | \eta \rangle$ at different times show opposing trends for the two models. The overall magnitude of the AMC curve is seen to decrease as the ignition time, τ_{ign}, is approached, while the overall magnitude of the inhomogeneous model is seen to increase as τ_{ign} is approached. It should be noted that the unconditional value of scalar dissipation rate, $\tilde{\chi}$, increases with time at L_{ign} for both models. The cause of this difference in CSDR predictions is largely due to the interaction between the flowfield and the formulation of the model. With the

AMC model, this interaction leads to a net decrease of the magnitude of the curve, while still providing an increase in $\tilde{\chi}$. The inhomogeneous model demonstrates the opposite trend, where the model formulation yields a net increase in the magnitude of the CSDR curve. As can be seen in Fig. 7b and c, the shape of CSDR provided by both mixing models is similar. Both models predict what is approximately a bell-shaped distribution; however, the peak for the inhomogeneous model is predicted slightly rich of $\eta = 0.5$, yielding an asymmetric profile. In the area lean of $\eta = 0.05$, the inhomogeneous model provides only small changes in $\langle \chi | \eta \rangle$ values as time progresses. Conversely, with the AMC model, the magnitude of $\langle \chi | \eta \rangle$ in this region decreases proportional to the peak value on the curve, as its shape is defined by a single function, $G(\eta)$. Therefore, the AMC model indicates that the turbulent mixing varies more strongly in time.

Through examining $\langle \chi | \eta \rangle$ for both models leading up to and at the time of ignition, the reasons for the reduced L_{ign} values predicted by the inhomogeneous model can be explained by examining the temporal $\langle \chi | \eta \rangle$ evolution. The nature of the AMC model and the fixed shape of the $\langle \chi | \eta \rangle$ distribution provides unexpected behaviour:

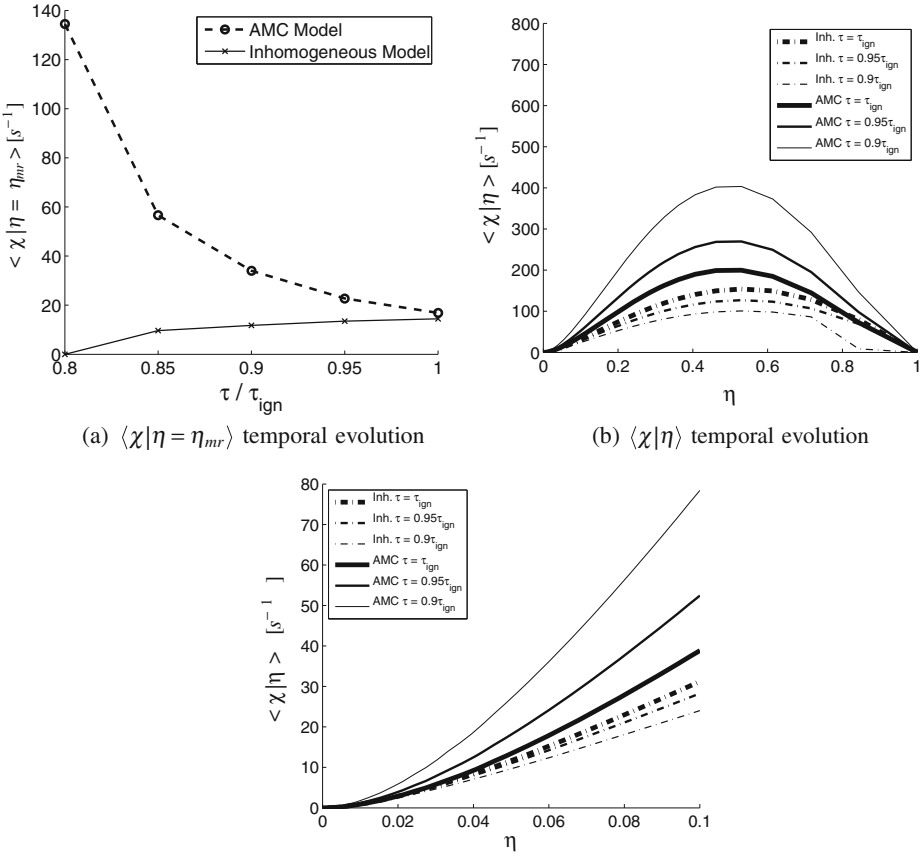

(a) $\langle \chi | \eta = \eta_{mr} \rangle$ temporal evolution

(b) $\langle \chi | \eta \rangle$ temporal evolution

(c) $\langle \chi | \eta \rangle$ temporal evolution, $0 \leq \ \leq 0.1$

Fig. 7 $\langle \chi | \eta \rangle$ evolution at L_{ign} for $T_{\text{coflow}} = 980\text{K}$

leading up to the point of ignition, the magnitude of $\langle \chi | \eta \rangle$ decreases with increasing τ, while the unconditional scalar dissipation rate increases with increasing time. The inhomogeneous model displays the opposite trend, with the magnitude of $\langle \chi | \eta \rangle$ increasing with τ, consistent with the trend of $\tilde{\chi}$. At low T_{coflow}, the overall increased mixing provided with the AMC model delays ignition at locations which support autoignition with the inhomogeneous model. At high T_{coflow}, despite the differences in predicted $\langle \chi | \eta = \eta_{\text{mr}} \rangle$, little difference in L_{ign} is observed due to the increasing magnitude of the chemical source term in the CMC equation.

4.3.3 Conditional scalars

As the predictions of $\langle \chi | \eta \rangle$ directly affect the chemistry calculations, examining the predictions of conditional species mass fractions is a direct indication of the performance of the inhomogeneous and AMC mixing models. This section provides a comparison of the conditional scalar values, specifically Y_{OH} and T, taken at the ignition location. In this comparison, the $T_{\text{coflow}} = 980$ K scenario is again used, with plots taken 0.02ms prior to ignition, or $\tau/\tau_{\text{ign}} \approx 0.95$, as well as at the time of ignition. In order to aid in the interpretation of the conditional scalar predictions, $\langle \chi | \eta \rangle$ for both the AMC and inhomogeneous mixing model can be used as a reference, shown previously in Fig. 7b and c. The conditional OH mass fraction, $\langle Y_{\text{OH}} | \eta \rangle$, is an important precursor to ignition. In Fig. 8a, the $\langle Y_{\text{OH}} | \eta \rangle$ values from both models are presented. At both times shown, the inhomogeneous model predicts a higher level of OH radicals present in the flow. This is an indication that the lower $\langle \chi | \eta \rangle$ leading up to ignition predicted by the inhomogeneous model allows for an earlier buildup of the concentration of intermediate radicals. The larger peak OH concentration for the inhomogeneous model is also an indication of the lower overall $\langle \chi | \eta \rangle$ at the time of ignition.

Although the calculations of $\langle T | \eta \rangle$ occur following the chemistry calculation, the predicted values nonetheless yield an indication of the overall chemical activity

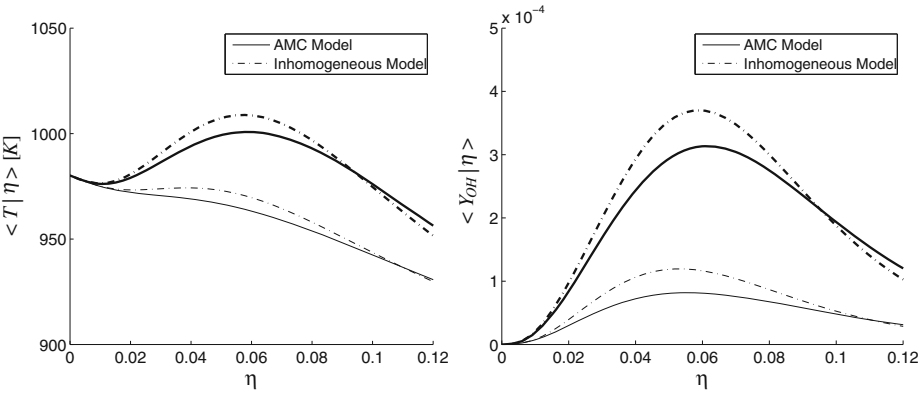

Fig. 8 Conditional values at $\tau/\tau_{\text{ign}} = 0.95$ (*thin lines*) and at the time of ignition (*thick lines*), all taken at L_{ign}

occurring at a given location, without investigating each individual species separately. Figure 8b indicates that the $\langle T|\eta\rangle$ trends closely follow the $\langle Y_{OH}|\eta\rangle$ seen in Fig. 8a. Again, the lower predictions of $\langle\chi|\eta\rangle$ made by the inhomogeneous model allow increased chemical activity and increased conditional temperatures in comparison to what is seen with the AMC model. The buildup of $\langle T|\eta\rangle$ appears once again to be more gradual due to the steady increase of $\langle\chi|\eta\rangle$, while the AMC model predicts a peak $\langle\chi|\eta\rangle$ occurring before ignition, which further delays the onset of ignition.

The trends seen in the conditional values further substantiate the trends indicated previously in Fig. 7, with a steady increase of $\langle\chi|\eta=\eta_{mr}\rangle$ predicted with the inhomogeneous model and a peak, then rapid decrease of $\langle\chi|\eta=\eta_{mr}\rangle$ predicted with the AMC model. The high levels of mixing provided by the AMC model delays chemical activity and affects the values of conditional scalars leading up to ignition. This provides insight into why the predictions of L_{ign} are larger than those produced with the inhomogeneous model.

4.4 Comparison with experimental data and previous simulation results

Figure 9a presents the current predicted ignition lengths compared with the experimental data [9] and previous numerical results using RANS-CMC [12], RANS-PDF [13] and LES-PDF [14, 15]. AMC is kept for the present comparisons due to small differences in the ignition prediction lengths between the AMC and the inhomogeneous model. It should be noted that the ignition lengths are determined in a similar fashion in [12] and [15] as in the present work, i.e this is the axial distance from the nozzle exit to the point of ignition at a given instant, whereas in [13], the ignition length is taken from steady-state calculations. There are only five experimental points measured for statistically steady regime and all situated in the random spots regime [9]. In the present study, the temperature dependence of the ignition lengths is well reproduced. Overall, the predicted ignition lengths are lower than the values given experimentally and in previous numerical work,

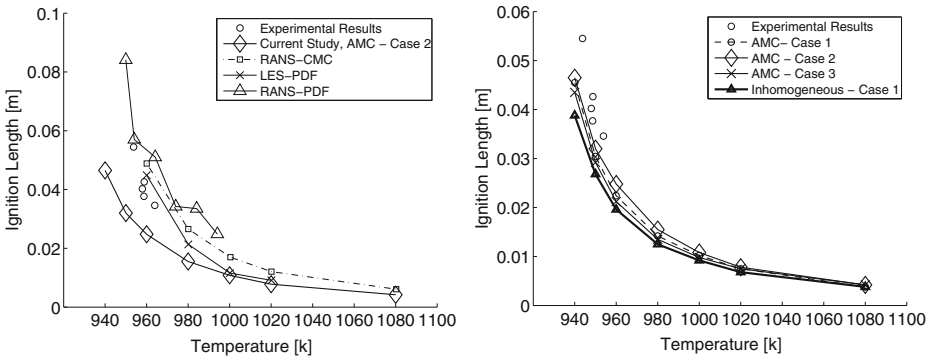

Fig. 9 **a** Ignition length comparison for present study alongside previous numerical work [12, 13, 15] and **b** Ignition length comparison for AMC and Inhomogeneous mixing model with different mixing constants, experimental results shifted by −10 K in the graph only

particularly at lower T_{coflow} as the no-ignition limit is approached. Compared to results of Lee and Mastorakos [13], the discrepancies may be explained by different mixing models used in the PDF transport equation in [13]. In previous RANS-CMC [12], same ignition criterion and chemical kinetics are used as in the present study. However, the modified constants in the k-ϵ are quite different probably leading to a different turbulent flow and mixing field. The LES performed by Jones et al. [14, 15] also include the same chemistry but, LES is expected to provide a more accurate description of the turbulent flow compared to RANS. In order to take into account the stated experimental error on coflow temperature (estimated to be approximately 10 K [9]) the experimental data points are shifted by 10K to the left in Fig. 9b). With this shift, it is found that the numerical results from the present study provide improved agreement with the experimental results, with only slight underpredictions. For example, at $T_{\text{coflow}} = 940$ K the autoignition length is underpredicted by approximately 17 %, while at $T_{\text{coflow}} = 950$ K there is an underprediction of approximately 19 %. The slope of the experimental results is closely matched, indicating that the trends seen numerically are a good representation of the actual physical processes occurring. With this shift, the differences between the current predictions and those from previous numerical results [12, 13, 15] are also much smaller.

In addition to the transient autoigniting properties of the flow, further study is performed on propagation of the flame after the initial ignition event. Prediction of different experimental regimes, such as flashback, lifted flame and random spots [9], are an important criteria in which to judge the overall performance of the present numerical models used. In order to investigate the final position of steady flames relative to the autoignition location, each T_{coflow} scenario is run to steady state using the inhomogeneous mixing model. Although detailed results are not presented for each simulation, the final flame structure of several representative cases is shown in a temperature plot of the 2D domain in Fig. 10. At the highest coflow temperature used, $T_{\text{coflow}} = 1080$ K, shown on the left in Fig. 10, ignition occurs off centre, and a fully attached flame forms on the fuel inlet. This corresponds to the flashback regime seen experimentally [9], where it was observed that autoignition occurred downstream of the fuel inlet, and due to the high temperature of the coflow, the flame structure was able to progress upstream and become fully attached to the fuel inlet. This is an indication that given the strength of the chemical source term, the diffusion terms in the CMC equation are able to overcome convection and mixing effects, and progress upstream to the edge of the mixing boundary between the fuel and oxidiser. Despite the strength of mixing near the inlet, the magnitude of the chemical source term can balance with the mixing term and sustains ignition at this location.

At lower T_{coflow}, such as 980 K shown in the centre of Fig. 10, the ignition location is observed to occur at the domain centreline, and a lifted flame is observed to form. The conditions along the centreline are more favourable for ignition at lower T_{coflow} when the autoignition process is mixing controlled and peak $\tilde{\chi}$ occurs in the mixing layer off centre. Ignition on the centreline is also observed in the simulations performed by Lee and Mastorakos [13]. At higher T_{coflow} when mixing has less impact on autoignition, the increased $\tilde{\chi}$ in the mixing layer is not seen to preclude ignition and the kernel location forms slightly off centre. The position of the lifted flame is slightly upstream, approximately 1d-2d, of the ignition location. The flame stabilises

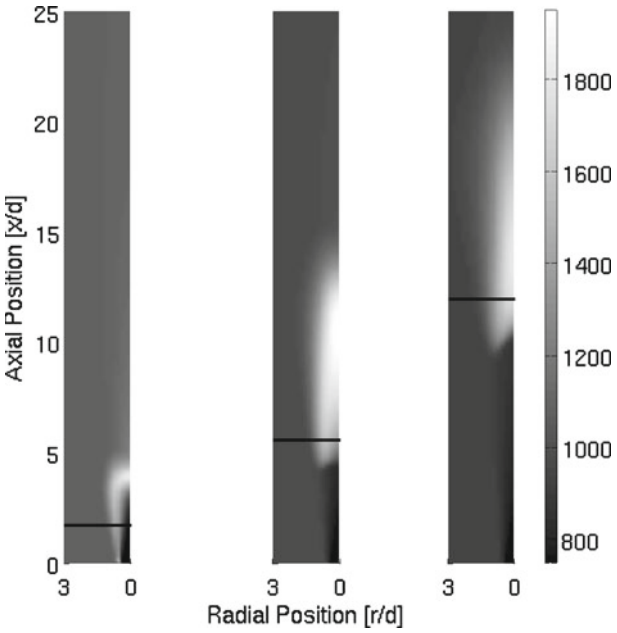

Fig. 10 Steady flame $\tilde{T}$ [K] predictions, $T_{\text{coflow}} = 1080$ K on the *left*, $T_{\text{coflow}} = 980$ K in the *centre*, $T_{\text{coflow}} = 950$ K on the *right*, with *solid black line* indicating the ignition length

further downstream at an axial location of approximately 4d from the inlet compared to the case of 1080 K.

As the temperature is further decreased, shown with $T_{\text{coflow}} = 950$ K on the right of Fig. 10, the ignition location is seen to move further downstream, while remaining on the domain centreline. Following ignition, the flame progresses upstream approximately 2d-3d from the initial ignition location. Similar to the $T_{\text{coflow}} = 980$ K case, this is an indication that, although the initial autoignition process requires additional time and axial distance, the spatial diffusive term in the CMC equation is sufficiently strong that the flame is able to proceed upstream. The flame structure is similar to the $T_{\text{coflow}} = 980$ K case, however, the burning region of the flame is slightly larger and lower temperatures are attained. Stabilisation of the flame further downstream is due to the chemical source term in Eq. 2 becoming weaker at lower temperatures, and the balance with the mixing term occurring further from the inlet where the level of mixing is reduced.

The lifted flame regime is successfully reproduced in the current study, however the random spots regime is not observed to occur for the present range of coflow temperature. It is believed that the averaging used in the RANS formulation of the CMC equations dampens the fluctuations leading to the absence of the random spots predictions. At the lowest temperature tested in this study, $T_{\text{coflow}} = 940$ K, a steady lifted flame is still observed to form after the ignition of a single parcel of fluid. It is believed that temperatures below 940K are close to the no ignition region, as $\langle \chi | \eta = \eta_{\text{mr}} \rangle$ approaches 0 as the temperature is decreased, indicating that the chemical source term is decreasing. T_{coflow} below 940 K are not tested in the current study.

5 Conclusions

This study outlined the implementation and performance of a finite volume discretised, fully coupled RANS based CFD/CMC code. Characterisation of the mixing field was presented to quantify the effects of modifying mixing constants. Two separate mixing models were implemented and compared, and the resulting ignition properties and flame structures were examined. A dynamic CMC grid was implemented to reduce computational expense. The major conclusions are:

- The modification of the mixing constants (C_{ϵ_1} and the Sc_t) had a visible effect on the formation of the steady turbulent mixing field: reducing C_{ϵ_1} to 0.40 from 1.40 yielded an increase in centreline $\widetilde{\xi''^2}$ and therefore $\tilde{\chi}$, while reducing Sc_t to 0.5 from 0.7 yield a reduction in centreline $\widetilde{\xi''^2}$ and therefore $\tilde{\chi}$. Although further validation cannot be made without access to additional experimental results, these trends provide insight into the sensitivity of RANS mixing constants when used in similar diffusive flows.
- Autoignition results were not very sensitive to changes in the turbulent mixing field due to different values of turbulence constants in the present conditions. The choice of turbulence constants only changed predicted ignition length by approximately 5 % when applied to the AMC mixing model.
- Predictions of ignition length performed by the inhomogeneous model were lower than those of the AMC model by up to 15 %. The difference in predictions between the models decreased as the magnitude of the conditional chemical source term increased with increasing coflow temperatures. The inhomogeneous model results indicated that the difference in models was largely due to the magnitude of the $\langle \chi | \eta \rangle$ curve predicted. The AMC model predicted an early peak in the magnitude of the $\langle \chi | \eta \rangle$ curve, but the magnitude decreased with increasing $\tilde{\xi}$. The inhomogeneous model produced a slow ramp up of $\langle \chi | \eta \rangle$, increasing with $\tilde{\chi}$ as time progresses. The slow ramp up of $\langle \chi | \eta \rangle$ with the inhomogeneous model provided conditions more suitable for autoignition, while the AMC model $\langle \chi | \eta \rangle$ progression led to a delay in ignition. Further, the limited impact of the inhomogeneous turbulent model is also due to the fact that ignition always occurs at a CSDR much lower than the critical value. A gradient diffusion model for the conditional velocity may be investigated in the future to further evaluate the effect of the CSDR model in CMC on ignition properties.
- Good agreement with the experimental data was obtained, in particular when uncertainty on air coflow temperature was considered. This is consistent with the previous LES-CMC study for the same experiment [26]. Comparison with previous numerical results [12–15] showed some differences mainly due to different models used and/or computational details, but provided a reasonable agreement. Formation of a full flame after the occurrence of an autoignition kernel reflected the physical phenomena occurring within the experiment, with two of the four experimentally observed regimes reproduced by use of the inhomogeneous mixing model. Further improvement may be achieved by considering LES to simulate the turbulent flow and mixing fields.

Acknowledgement This work is supported by NSERC (Natural Sciences and Engineering Research Council), Canada and Ontario Research Funds (ORF).

References

1. Mastorakos, E.: Ignition of turbulent non-premixed flames. Prog. Energy Combust. Sci. **25**, 57–97 (2009)
2. Pitsch, H., Barths, H., Peters, N.: Three-dimensional modeling of NOx and soot formation in DI-diesel engines using detailed chemistry based on the interactive—amelet approach. Technical report, SAE (1996)
3. Klimenko, A.Yu., Bilger, R.W.: Conditional moment closure for turbulent combustion. Prog. Energy Combust. Sci. **25**(6), 595–687 (1999)
4. Huang, J., Bushe, W.K.: Simulation of transient turbulent methane jet ignition and combustion under engine-relevant conditions using conditional source-term estimation with detailed chemistry. Combust. Theory Model. **11**, 977–1008 (2007)
5. Michel, J.B., Colin, O., Veynante, D.: Comparison of differing formulations of the PCM model by their application to the simulation of an auto-igniting H2/air jet. Flow Turbul. Combust. **83**, 33–60 (2009)
6. Echekki, T., Gupta, K.G.: Hydrogen autoignition in a turbulent jet with preheated co-flow air. Int. J. Hydrogen Energy **34**, 8352–8377 (2009)
7. Jones, W.P., Navarro-Martinez, S.: Large eddy simulation of autoignition with a subgrid probability density function method. Combust. Flame **150**(3), 170–187 (2007)
8. Echekki, T., Chen, J.H.: Direct numerical simulations of auto-ignition in non-homogeneous hydrogen-air mixtures. Combust. Flame **134**, 169–191 (2003)
9. Markides, C.N., Mastorakos, E.: An experimental study of hydrogen autoignition in a turbulent co-flow of heated air. Proc. Combust. Inst. **30**, 883–891 (2005)
10. Stanković, I., Triantafyllidis, A., Mastorakos, E., Lacor, C., Merci, B.: Simulation of hydrogen auto-ignition in a turbulent co-flow of heated air with les and CMC approach. Flow Turbul. Combust. **86**, 689–710 (2011)
11. Kerkemeier, S.G.: Direct numerical simulation of combustion on petascale platforms: application to turbulent non-premixed hydrogen autoignition. PhD thesis, ETH Zurich, Zurich, Switzerland (2010)
12. Patwardhan, S.S., Lakshmisha, K.N.: Autoignition of turbulent hydrogen jet in a co-flow of heated air. Int. J. Hydrogen Energy **33**, 7265–7263 (2008)
13. Lee, C.W., Mastorakos, E.: Transported scalar PDF calculations of autoignition of a hydrogen jet in a heated turbulent co-flow. Combust. Theory Model. **12**, 1153–1178 (2008)
14. Jones, W.P., Navarro-Martinez, S.: Study of hydrogen auto-ignition in a turbulent air co-flow using a large eddy simulation approach. Comput. Fluids **37**, 802–808 (2008)
15. Jones, W.P., Navarro-Martinez, S., Rohl, O.: Large eddy simulation of hydrogen auto-ignition with a probability density function method. Proc. Combust. Inst. **31**, 1765–1771 (2007)
16. Markides, C.N., De Paola, G., Mastorakos, E.: Measurements and simulations of mixing and autoignition of an n-heptane plume in a turbulent flow of heated air. Exp. Therm. Fluid Sci. **31**, 393–401 (2007)
17. Girimaji, S.S.: Assumed beta-pdf model for turbulent mixing, validation and extension to multiple scalar mixing. Combust. Sci. Technol. **78**(4–6), 177–196 (1991)
18. O'Brien, E., Jiang, T.L.: The conditional dissipation rate of an initially binary scalar in homogeneous turbulence. Phys. Fluids A **3**(12), 3121–3123 (1991)
19. Devaud, C.B., Bilger, R.W., Liu, T.: A new method of modeling the conditional scalar dissipation rate. Phys. Fluids **16**(6), 2004–2011 (2004)
20. Mortensen, M.: Consistent modeling of scalar mixing for presumed, multiple parameter probability density functions. Phys. Fluids **17**(018106) (2005)
21. Kent, J.H., Kronenburg, A., Bilger, R.W.: Computation of conditional average scalar dissipation in turbulent jet diffusion flames. Flow Turbul. Combust. **64**, 145–159 (2000)
22. Cleary, M.J., Kent, J.H.: Modelling of species in hood fires by conditional moment closure. Combust. Flame **143**, 357–368 (2005)
23. Sreedhara, S., Lee, Y., Huh, K.Y., Ahn, D.H.: Comparison of submodels for conditional velocity and scalar dissipation in CMC simulation of piloted jet and bluff-body flames. Combust. Flame **152**, 282–286 (2007)
24. Rogerson, J.W., Kent, J.H., Bilger, R.W.: Conditional moment closure in a bagasse-fired boiler. Proc. Combust. Inst. **31**, 2805–2811 (2007)
25. Milford, A., Devaud, C.B.: Investigation of an inhomogeneous turbulent mixing model for conditional moment closure applied to autoignition. Combust. Flame **157**, 1467–1483 (2010)

26. Stanković, I.: Numerical simulations of hydrogen auto-ignition in turbulent flows. PhD thesis, University of Ghent, Ghent, Flanders, Belgium (2011)
27. Kim, S.H., Huh, K.Y., Fraser, R.A.: Numerical prediction of the autoignition delay in a diesel–like environment by the conditional moment closure model. Proc. Combust. Inst. **28**, 185–191 (2000)
28. El Sayed, A., Devaud, C.B.: Conditional moment closure (CMC) applied to autoignition of high pressure methane jets in a shock tube. Combust. Theory Model. **12**(5), 943–972 (2008)
29. El Sayed, A., Milford, A., Devaud, C.B.: Modelling of autoignition for methane-based fuel blends using conditional moment closure. Proc. Combust. Inst. **32**(1), 1621–1628 (2009)
30. Kim, W.T., Huh, K.Y.: Numerical simulation of spray autoignition by the first-order conditional. Moment closure model. Proc. Combust. Inst. **29**, 569–576 (2002)
31. Wright, Y.M., De Paola, G., Boulouchos, K., Mastorakos, E.: Simulations of spray autoignition and flame establishment with two-dimensional CMC. Combust. Flame **143**(4), 402–419 (2005)
32. Borghesi, G., Mastorakos, E., Devaud, C.B., Bilger, R.W.: Modeling evaporation effects in conditional moment closure for spray autoignition. Combust. Theory. Model. **15**, 725–752 (2011)
33. De Paola, G., Kim, I.S., Mastorakos, E.: Second-order conditional moment closure simulations of autoignition of an n-heptane plume in a turbulent coflow of heated air. Flow Turbul. Combust. **82**, 455–475 (2009)
34. Kuznetsov, V.R., Sabel'Nikov, V.A.: Turbulence and Combustion. Hemisphere, New York (1990)
35. Pope, S.B.: Pdf methods for turbulent reactive flows. Prog. Energy Combust. Sci. **11**(2), 119–192 (1985)
36. Cleary, M.: CMC modelling of enclosure fires. PhD thesis, University of Sydney, Sydney, Australia (2004)
37. Pope, S.B.: Turbulent Flows. Cambridge University Press, Cambridge (2000)
38. Peters, N.: Turbulent Combustion. Cambridge University Press, Cambridge (2000)
39. Janicka, J., Peters, N.: Prediction of turbulent jet diffusion flame lift-off using a pdf transport equation. Proc. Combust. Inst. **19**, 367–374 (1982)
40. Patankar, S.V.: Numerical Heat Transfer and Fluid Flow. Taylor & Francis Group, New York (1980)
41. Spalding, D.B.: A novel finite-difference formulation for differential expressions involving both first and second derivatives. Int. J. Numer. Methods **4**, 551–559 (1972)
42. Devaud, C.B., Bray, K.N.C.: Assessment of the applicability of conditional moment closure to a lifted turbulent flame. First order model. Combust. Flame **132**(1), 102–114 (2003)
43. Jones, W.P., Launder, B.E.: The prediction of laminarization with a two-equation model of turbulence. Int. J. Heat Mass Transfer **15**(2), 301–314 (1972)
44. Launder, B.E., Sharma, B.I.: Application of the energy-dissipation model of turbulence to the calculation of flow near a spinning disc. Lett. Heat Mass Transfer **1**, 131–138 (1974)
45. Brown, P.N., Byrne, G.D., Hindmarsh, A.C.: VODE: a variable-coefficient ODE solver. Technical report, Lawrence Livermore National Laboratory (1988)
46. Yetter, R.A., Dryer, F.L., Rabitz, H.: A comprehensive reaction mechanism for carbon monoxide / hydrogen / oxygen kinetics. Combust. Sci. Technol. **79**, 97–128 (1991)
47. Stanković, I., Merci, B.: Analysis of auto-ignition of heated hydrogen-air mixtures with different detailed reaction mechanisms. Combust. Theory. Model. **15**, 409–436 (2011)
48. Malalasekra, W., Versteeg, H.K.: An Introduction to Computational Fluid Dynamics, The Finite Volume Method. Pearson Education Limited (2007)
49. Pope, S.B.: An explanation of the turbulent round-jet/plane-jet anomaly. AIAA **16**(3), 279–281 (1978)
50. Masri, A.R., Cao, R., Pope, S.B., Goldin, G.M.: PDF calculations of turbulent lifted flames of h2/n2 issuing into a vitiated co-flow. Combust. Theory Model. **8**, 1–22 (2004)
51. Buckrell, A.: Investigation of mixing models for finite volume conditional moment closure applied to autoignition of hydrogen jets. Master's thesis, University of Waterloo (2012)